Mirrors of Bonding in Metal Halide Perovskites

Maarten G. Goesten*[ID] and Roald Hoffmann*[ID]

Department of Chemistry and Chemical Biology, Cornell University, 259 East Avenue, Ithaca, New York 14853-1301, United States

S *Supporting Information*

ABSTRACT: We explore the chemical bonding and band gap in the metal halide perovskites ABX_3 (where A is a cation, B a metal dication, and X a halide) through detailed calculations and a qualitative, symmetry-based bonding analysis that moves between chemical and physical viewpoints, covering every aspect of bonding over a range of 15 eV around the band gap. We show how the gap is controlled by metal–halide orbital interactions that give rise to a characteristic mirror of bands, a bonding signpost which first shows up in turning on and off the scalar relativistic effects in computation of the band structure of $CsPbBr_3$. The mirror is made up by a Pb *6s* and Br *4p* combination that moves in an understandable way through the Brillouin zone, setting the valence band maximum. The mirror is also there when the A cation is changed to an organocation and is robust enough to persist through moderate distortions of the lattice. The analysis predicts how a modification of Pb^{2+} to Sn^{2+} and Ge^{2+} and a variation of the halide X influence the band gap. In describing in equal detail the lowest three conduction bands, a second mirror of bonding emerges. For $CsPbBr_3$, this mirror is made up by Pb *6p* and Br *4p* combinations. An understanding of the way these combinations move in reciprocal space to set the conduction band minimum allows us to see why the band gap is direct. The orbital analysis provides a chemical and intuitive picture of band gap engineering in this popular class of materials.

INTRODUCTION

Perovskites are a familiar class of crystalline solids with the generic formula ABX_3, where A and B are cations and X is an anion. Perovskites are old, even to human beings.[1] And they are new—meaning that our interest in them, as documented by the literature, has grown tremendously in recent times.[2−5] Two classes of perovskites dominate the thousands of articles studying this group of extended structures: those with X = oxide, and those with X = halide. In this first paper, we will focus on the halide class, which is responsible for the booming interest of late, much related to a potential in outperforming silicon-based technology in photovoltaics. In a second paper we will analyze the bonding in the oxide perovskites and unravel the similarities and differences between the two classes. Our perspective will cross physics and materials science, using the full apparatus of band theory, but we will also build a bridge with chemistry. The aim is a connection that will allow people to systematically relate chemical bonding to band gap (and other characteristics) within the perovskite ABX_3 structure, and to rationally design materials with targeted properties.

The cubic perovskite archetype (space group $Pm\overline{3}m$) is shown in Figure 1. The lattice vectors a_1, a_2, and a_3 lie parallel to the vertices of the conventional unit cell, a cube (structure 2). The simple cubic structure deforms in a myriad of ways[6−8]—we will eventually look at some of these, but we begin in the most symmetrical structure. The coordination environment is octahedral for the B ions—in fact, the structure is just as easily described as built from corner- or vertex-sharing

BX_6 octahedra (structure 3). The coordination of the A ions is cuboctahedral in X, cubic in B. The X ions are usually seen as two-coordinate, yet one could worry about X−A interactions (among others).

In general, stable perovskites follow stoichiometries that relate to common oxidation states. For the halides, in ABX_3, A is typically a monovalent cation, B a divalent cation (such as Pb^{2+}), and X a monovalent anion, typically Br$^-$ or I$^-$.

RESULTS AND DISCUSSION

Cubic $CsPbBr_3$. Even though the A cation does not contribute to bands near the Fermi level (as we will see), its size and shape are important for the symmetry, stability, and properties of the halide perovskite material.[9] In all-inorganic halide perovskites, Cs$^+$ is the popular choice for A. The so-called hybrid organic−inorganic variants typically contain methylammonium ($CH_3NH_3^+$) or formamidinium (CH-$(NH_2)_2^+$) as the A ion. These organics improve separation of photocarriers upon photoexcitation, but the materials also suffer from a decrease in structural stability. A recent report suggests that the two effects are correlated.[10]

The lead bromide perovskite is known to take up the cubic $Pm\overline{3}m$ crystal structure in both $CsPbBr_3$ and CH_3NH_3-$PbBr_3$.[11−14] We begin with the simple, all-inorganic archetype $CsPbBr_3$, noting that this structure distorts toward tetragonal $P4/mbm$ at temperatures below 130 °C, and then ortho-
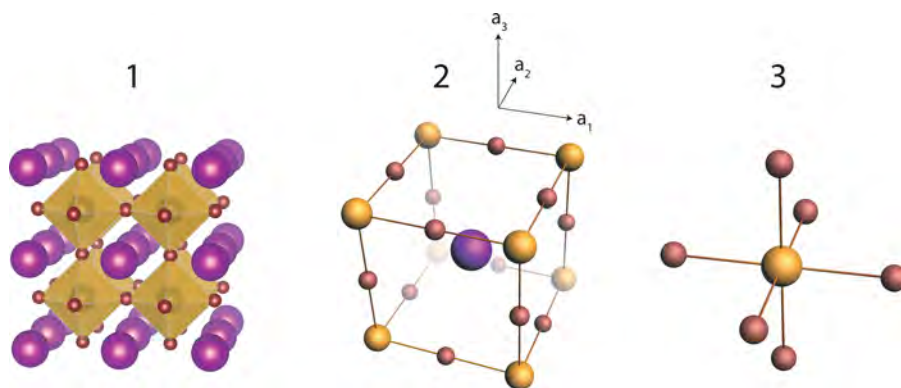
Figure 1. Three representations of the cubic ABX_3 perovskite structure: 1, the lattice with A in purple, B as yellow octahedra, and X in burgundy; 2, primitive/conventional unit cell of ABX_3; and 3, local octahedral environment around B.

rhombic *Pnma* below 88 °C. Figure 2 displays the structure optimized within cubic symmetry. The Pb–Br bond lengths are 3.0 Å, and all Br–Pb–Br angles are 90° or 180°.
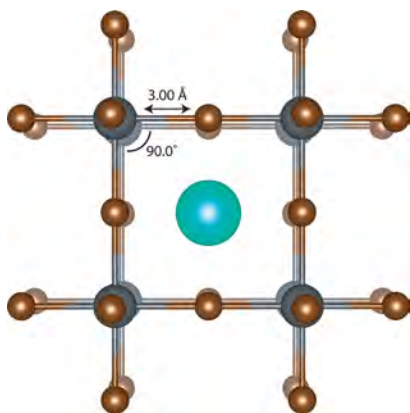

Figure 2. A view of the cubic structure of $CsPbBr_3$. Color code: Pb, gray; Br, brown; Cs, turquoise.

The computed band structure of ideally cubic $CsPbBr_3$ is shown in Figure 3; it is representative of a few hundred similar band structures in literature. The details of the present calculations, in which atomic Slater-type orbital (STO) basis sets were employed, can be found in the Computational

Methods section at the end of this paper. We note that the one-electron energy in this and all calculations is shown on an absolute energy scale, referenced against the vacuum level instead of the more typical Fermi level reference—comparison at absolute energies will be of some significance in our upcoming analysis.

On the right of the band structure in Figure 3, we have drawn the Brillouin zone (BZ) for the simple cubic lattice. This is the primitive cell in reciprocal space, and it contains all wave vectors k that yield plane waves $e^{ik \cdot r}$ with the periodicity of the cubic lattice. The BZ will become important later, when constructing crystal orbitals. For now, we introduce it both to show that it is also cubic—with reciprocal-lattice vectors b_1, b_2, and b_3 pointing to the same directions as a_1, a_2, and a_3—and to show the path across high-symmetry points along which the band energies run in the plot to its left. We are aware that a different path (Γ-X-M-Γ-R-X) is commonly used in other papers, but the reason for our choice will become apparent.

The plot features a characteristic highest occupied band that rises from $\Gamma \rightarrow X \rightarrow M \rightarrow R$, which sets a direct band gap. We proceed by analyzing the character of this band, the effect of relativity, and how both work in together in setting the valence band maximum.

The Role of Relativity. If one is going to have Pb in a structure, as we do in $CsPbBr_3$, one anticipates a relativistic effect on the orbitals of Pb, and perhaps also those of Cs. One
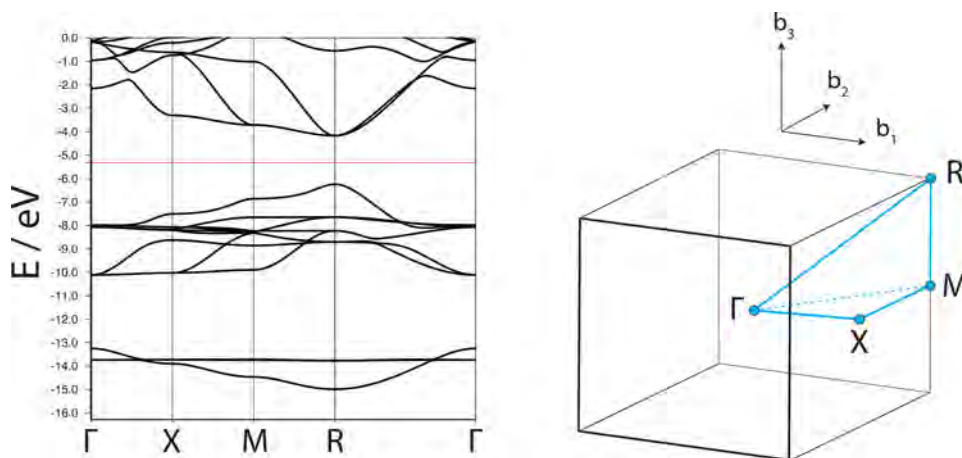

Figure 3. (Left) Band structure of $CsPbBr_3$ computed at the ZORA-SCAN/TZ2P level of theory. The one-electron energy is referenced to the vacuum level, and the Fermi level is indicated as a red line. (Right) The corresponding Brillouin zone of the simple cubic lattice.
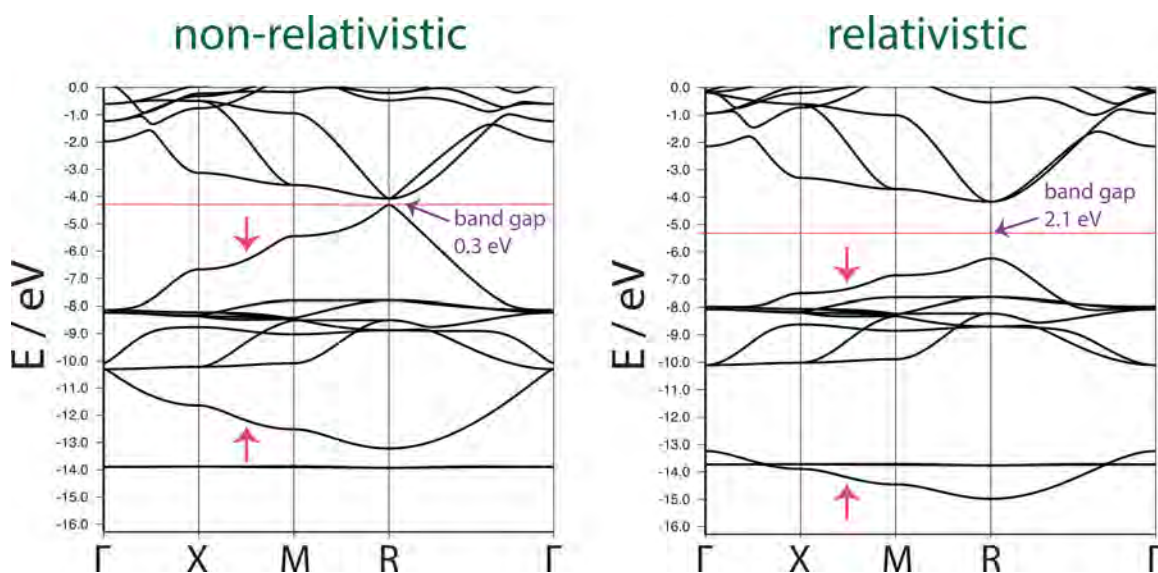
Figure 4. Band structure of CsPbBr$_3$, computed at SCAN/TZ2P (left) and ZORA-SCAN/TZ2P (right). The magenta arrows mark the mirrored bands.
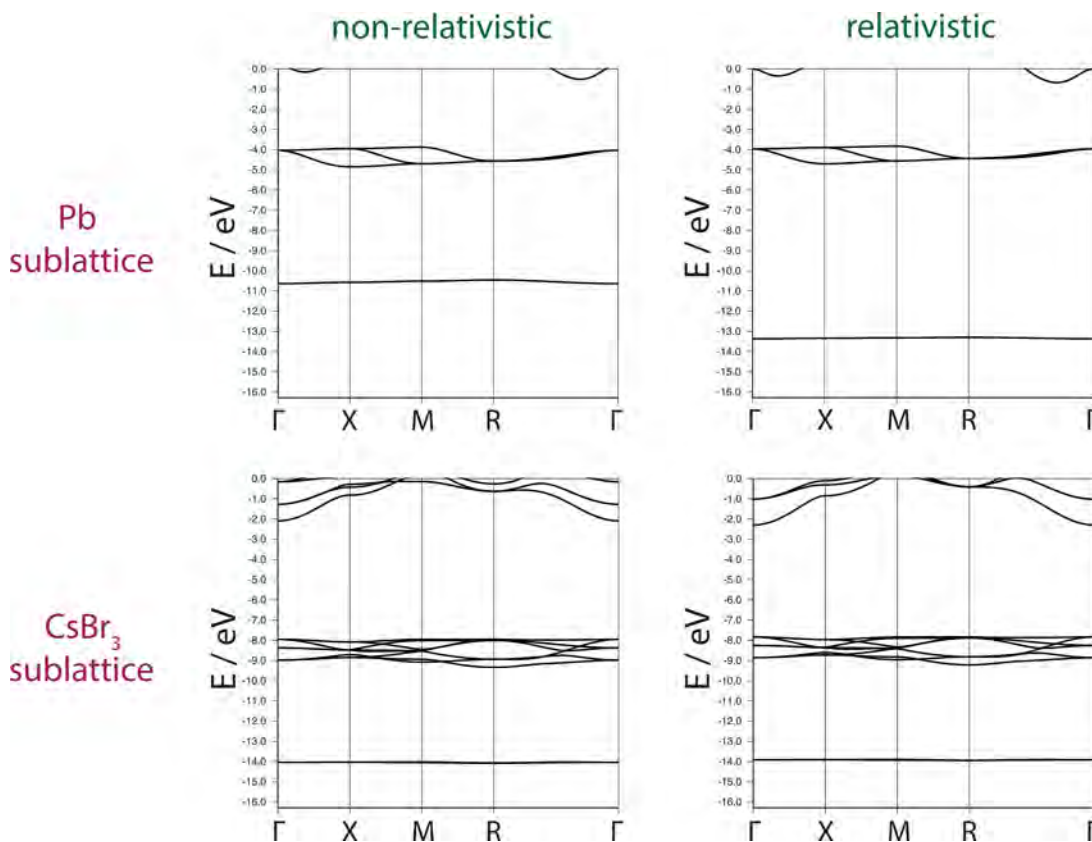

Figure 5. Computed band structures of the Pb and CsBr$_3$ sublattices in CsPbBr$_3$.

thing theory allows us to do is to probe the source of the underlying physics by computational experiments that are impossible to perform in reality. In the case at point this involves turning off the workings of scalar relativistic effects, herein approached by the zeroth-order regular approximation to the Dirac equation (ZORA).

Non-relativistic and relativistic band structure calculations are shown in Figure 4. What we see clearly in the left and right sides of Figure 4 are two occupied bands behaving in mirror-

like fashion—one going down $\Gamma \to X \to M \to R$ and rising back to Γ. The other, the highest occupied band, is doing precisely the opposite—it goes up along $\Gamma \to X \to M \to R$ and then down to Γ. The mirroring of these bands is not an accident, and while it occurs whether relativistic effects are included or not, relativity plays a major role in decreasing the bandwidth of both mirrored bands, thereby widening the band gap from 0.3 to 2.1 eV.
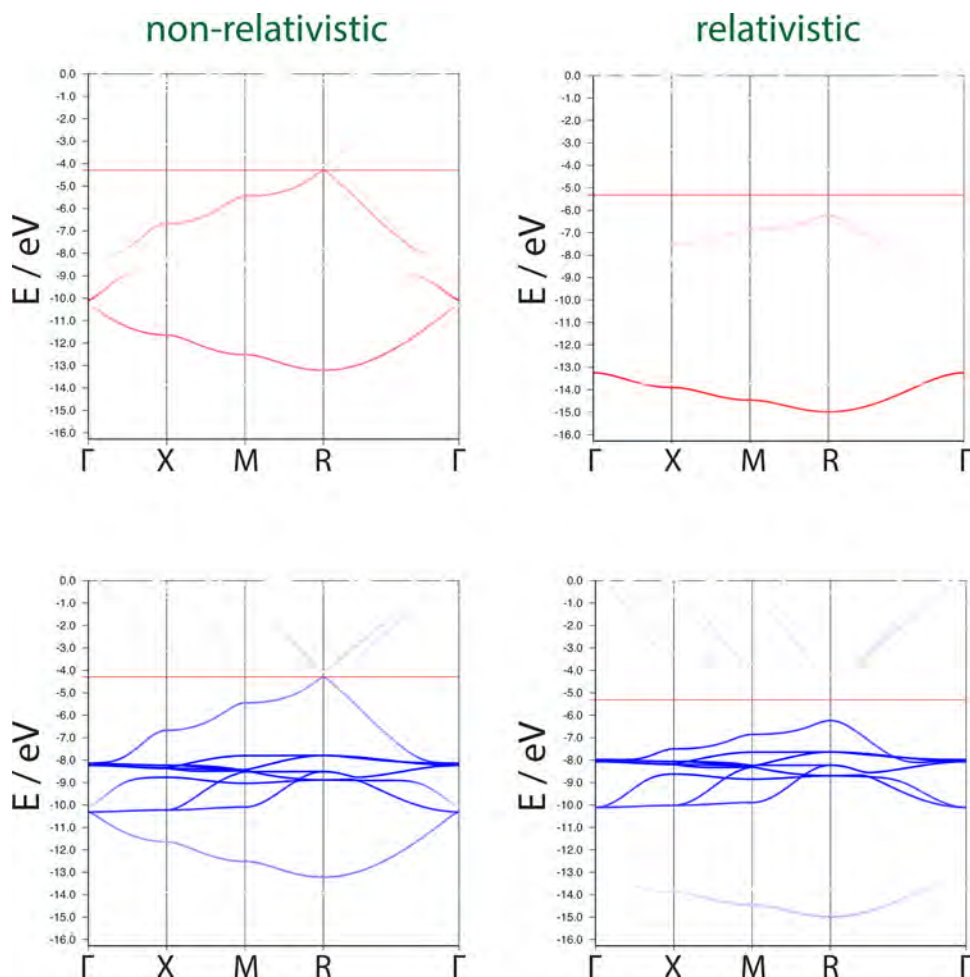
Figure 6. Pb *6s* (red, top) and Br *4p* (blue, bottom) contributions to the band structure of CsPbBr$_3$.

The fact that this difference in band gap is related to the effect of relativity on the Pb *6s* orbitals, and to Pb−Br interaction, we obtain that from calculations on the respective Pb and CsBr$_3$ sublattices. Their band structures are shown in Figure 5.

All pictured bands in the Pb sublattice are reasonably flat—the atoms are too sparsely spaced to feel one another. The lowest lying band in the Pb sublattice, and the flattest, belongs to the *6s* orbital. Relativistic effects bring it down by ca. 2.5 eV. The three Pb *p* bands have some bandwidth, and they run as we expect them to do in a simple cubic lattice.[15] Their position on the energy scale indicates that they will be mainly involved in making up the conduction bands in CsPbBr$_3$—established knowledge in the literature.

The CsBr$_3$ sublattice is more challenging to unfold. The easiest part involves the contribution by Cs, making up the flat bands at −14 eV. Those are Cs *5p* orbitals, sometimes viewed as outer-core or subvalence levels[16−18]—their energy is effectively unperturbed by relativity. The flatness indicates an absence of bonding between Cs and its surrounding scaffold, and renders the band an energy calibration for all other bands. The three bromides in the unit cell contribute three *4s* orbitals, which are below the energy window shown. Above them, roughly in the region −8 to −9 eV, are bands arising from nine Br *4p* orbitals, in a relatively narrow energy window.

The Mirror. We move back to the band structure of CsPbBr$_3$. It is clear from Figures 3 and 5 that Pb and Br are

interacting. Of their 10 levels in total (1 Pb *6s* and nine Br *4p*), eight remain in a 2-eV-wide band, while two others form the striking mirror pattern—one band going up, the other going down. What is the makeup of the mirrored bands?

Figure 6 displays the Pb *6s* contribution to all bands, in red, as well as the Br *4p* (together), in blue. These are obtained directly from the STO basis set. We see that the Pb *6s* orbital contributes significantly to the mirrored bands, mixing strongly (and exclusively) into both bands. We also see that the Pb *6s* contributes to both bands for the non-relativistic calculation, but relativity makes it contribute more to the band that runs down. Both bands also feature significant Br *p* character. The Br contributions are the inverse of the Pb ones—if relativistic effects are considered, one sees Br *p* character contributing more to the band that runs up.

Clearly, some combination of Br *4p* bands interacts strongly with the Pb *6s*, giving rise to the mirror. Figure 6, and several previous reports,[19−21] suggest that we look for the reason in Pb *6s*−Br *4p* σ combinations. We proceed by a step-by-step construction of the crystal orbitals that belong to the mirrored bands.

In Figure 1, structure 2, we had displayed a cell for cubic perovskites which is both primitive and conventional (it contains the point group symmetry of the overall lattice). For our upcoming construction, we require a different primitive cell, one that shares no atoms with any neighboring cell—this allows us to define an orbital basis for a single cell, from which
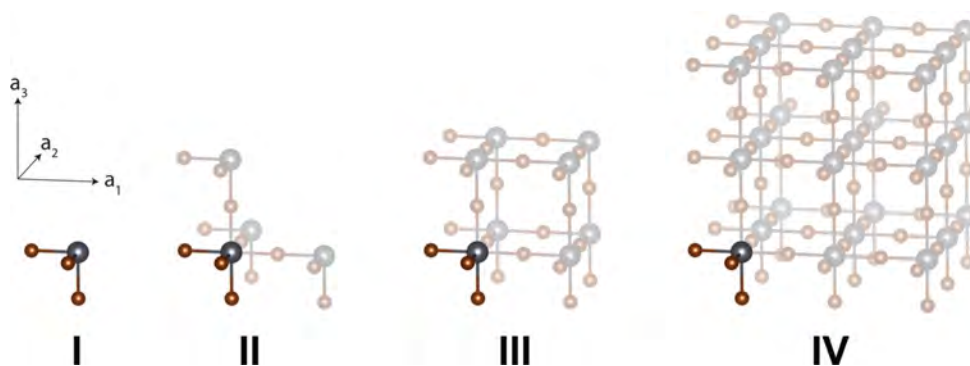
Figure 7. Cubic lattice build-up by a primitive $PbBr_3$ unit by translation through a_1, a_2, and a_3.

we can derive the crystal orbitals. Such a primitive cell is shown in Figure 7, where we demonstrate how it builds the cubic perovskite lattice by translation through vectors a_1, a_2, and a_3. We have omitted the nonbonding Cs ions.

The primitive cell contains a C_{3v}-symmetric $PbBr_3$ unit, for which we can construct a symmetry-adapted linear combination of Br p orbitals, suited for σ overlap with the Pb $6s$. This is a fragment molecular orbital (FMO) of a_1 symmetry within the point group of the basis. The interaction of this a_1 Br $4p$ combination with the Pb $6s$ gives rise to one σ and one σ^* molecular orbital (MO), shown in Figure 8. The unit is slightly

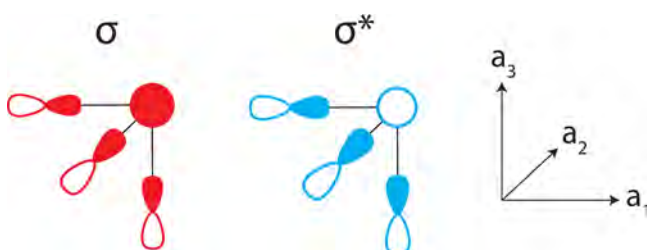**Figure 8.** σ and σ^* Pb $6s$/Br $4p$ combinations of a_1 symmetry (within the C_{3v} point group) for the $PbBr_3$ unit.

angled here (with respect to Figure 7), so as to provide us a better visual perspective of what these orbitals look like. Also, please note that we have assigned a schematically larger contribution in the σ combination to the Pb $6s$, which lies lower in energy than Br $4p$ (Figure 5), and vice versa for σ^*.[22] We will return to this aspect, a consequence of the nature of orbital interactions.

The σ and σ^* MO combinations of Figure 8 are bases from which we can construct crystal orbitals. We build these by translation of the MOs along the real-space vectors— analogous to what we did in Figure 7—while applying phase factors $e^{ik \cdot r}$ for the different high-symmetry points of the BZ. In that BZ (Figure 3), the high-symmetry points with their

reduced coordinates in reciprocal space are Γ $(0,0,0)$, X $(^1/_2,0,0)$, M $(^1/_2,^1/_2,0)$, and R $(^1/_2,^1/_2,^1/_2)$. At Γ, $b_1 = b_2 = b_3 = 0$; the orbitals propagate in 3D with no phase factor in any direction. At X, M, and R, the reciprocal-space vectors take either the value of 0 or 1/2.[23] The nonzero value for b_1, b_2, and b_3 corresponds to phase inversion of the MOs between adjacent unit cells in the direction of that reciprocal lattice vector. As b_1 points in the same direction as a_1, b_2 in the same direction as a_2, etc., we have phase inversion in the crystal orbitals along a_1 for X, along a_1 and a_2 for M, and a_1, a_2, and a_3 for R. We have drawn the first step in the construction of these crystal orbitals, with the σ combination as the orbital basis, in Figure 9.

If we zoom in on Figure 9, we may focus on one complete $PbBr_6$ octahedron that contains the basis, a chemically intuitive beacon. In Figure 10 we truncate the crystal orbitals of Figure 9 to this octahedron, in order to show the development in bonding along Γ-X-M-R for both the σ and σ^* bands. We can now move to the analysis of their band energies based on a calculus of bonding and antibonding interactions. At Γ, there are three bonding and three antibonding interactions for both the σ and σ^* bands. As we move to X, phase inversion replaces antibonding by bonding along one direction for σ; we are removing nodal planes, and introducing stabilization. The opposite happens for σ^*, where antibonding is starting to win out. Two identical phase-inversion operations farther, at R, the σ and σ^* bands have become as bonding and antibonding as they can be, and the level splitting is at its maximum. We have our mirror.

Figure 11 displays a density-of-states (DOS) plot, computed at the relativistic level. It is augmented by Crystal Orbital Overlap Populations (COOPs), which weight the DOS by the states' contribution to bonding or antibonding, as measured by a Mulliken overlap population analysis.[24] The DOS features a spike from the flat Cs bands below the Fermi level and several broader regions. We can relate the mirror bands to the blue bonding and antibonding $s^{Pb}-p^{Br}$ regions in the COOP (these
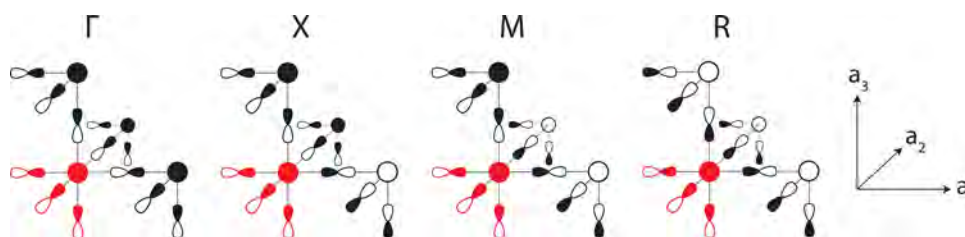

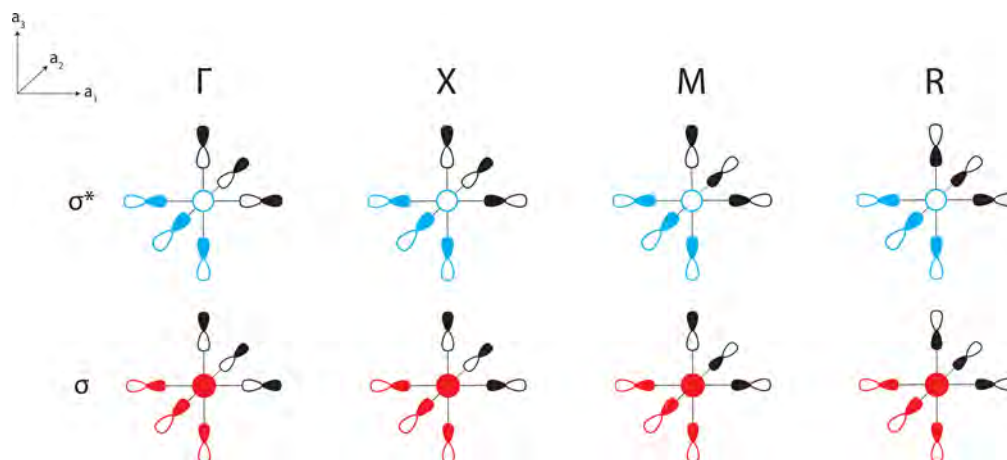**Figure 9.** Constructed crystal orbitals of the σ band at Γ, X, M, and R. The orbital basis is drawn in red.

Figure 10. σ and σ^* crystal orbitals along Γ-X-M-R, represented by a PbBr$_6$ octahedral unit. The orbital bases for the σ and σ^* bands are colored red and blue, respectively.
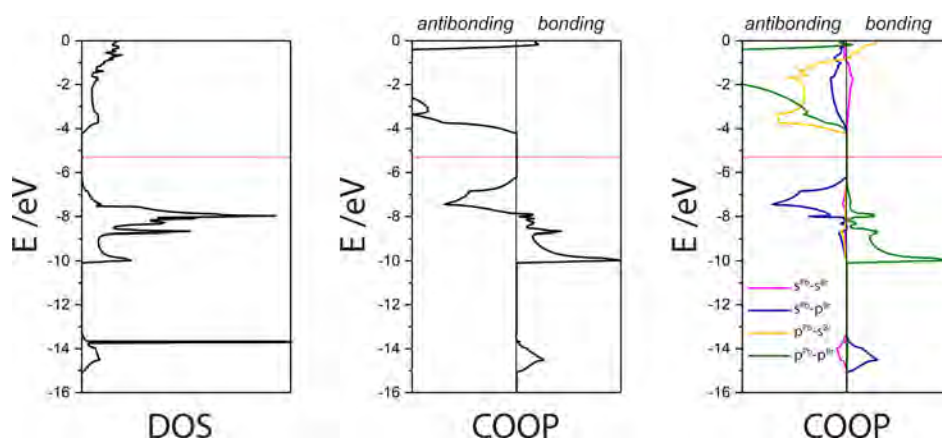

Figure 11. Density-of-states (left) and Crystal Orbital Overlap Population plots, cumulative (center) and decomposed into s-s, s-p, p-s, and p-p bonding contributions between Pb and Br (right).

regions shift predictably in a non-relativistic calculation; see Supporting Information (SI), Figure S1.

The green states between −7.5 and −10 eV are not involved in the mirror, yet they are hardly innocent of Pb−Br bonding. The COOP tells us that these involve $p^{Pb}-p^{Br}$ interaction. This important observation—which will direct us toward an understanding of the conduction band later—was also made in a report by Huang and Lambrecht, from their analysis of DOS contributions.[19] As we will see, these states form a second mirror.

Let us relate relativity to band gap and bonding in CsPbBr$_3$. We move back to Figure 4. Our calculations on the Pb sublattice there revealed that relativistic effects bring down the Pb 6s orbital by some 2.5 eV, to ca. −13.5 eV. This pushes it away from the Br 4p combinations, which lie all between −8 and −9 eV. As relativistic effects are turned on, the resonance in energy of the interacting orbitals is less pronounced, and the two-fold consequences—represented in the simple MO scheme of Figure 12—follow: (i) we obtain less stabilization by bonding, and less destabilization by antibonding, and (ii) we can anticipate the lower-lying orbital to contribute significantly more to the bonding level, and the higher-lying orbital significantly more to the antibonding level.[25]

Indeed, the bandwidths of the two mirrored bands are reduced by relativity, and the Pb 6s character moves to the lower band (Figure 6, red). This is how relativity and bonding
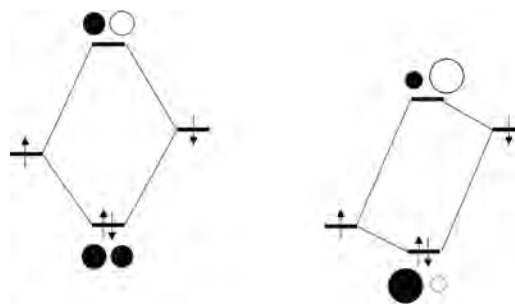

Figure 12. A schematic view of interaction between atomic orbitals of different energies.

work together to decrease the mirror's width and increase the band gap.

The analysis we present here could have been done in a more formal way, using the apparatus of group theory in the solid state. An excellent example of how this is done may be found in the Wolfram and Ellialtıoğlu analysis of the crystal orbitals of the oxide perovskites.[26,27]

We have chosen to focus on the details of orbital interactions and how they change within the BZ, because we feel a deeper physical understanding of the bonding ensues.

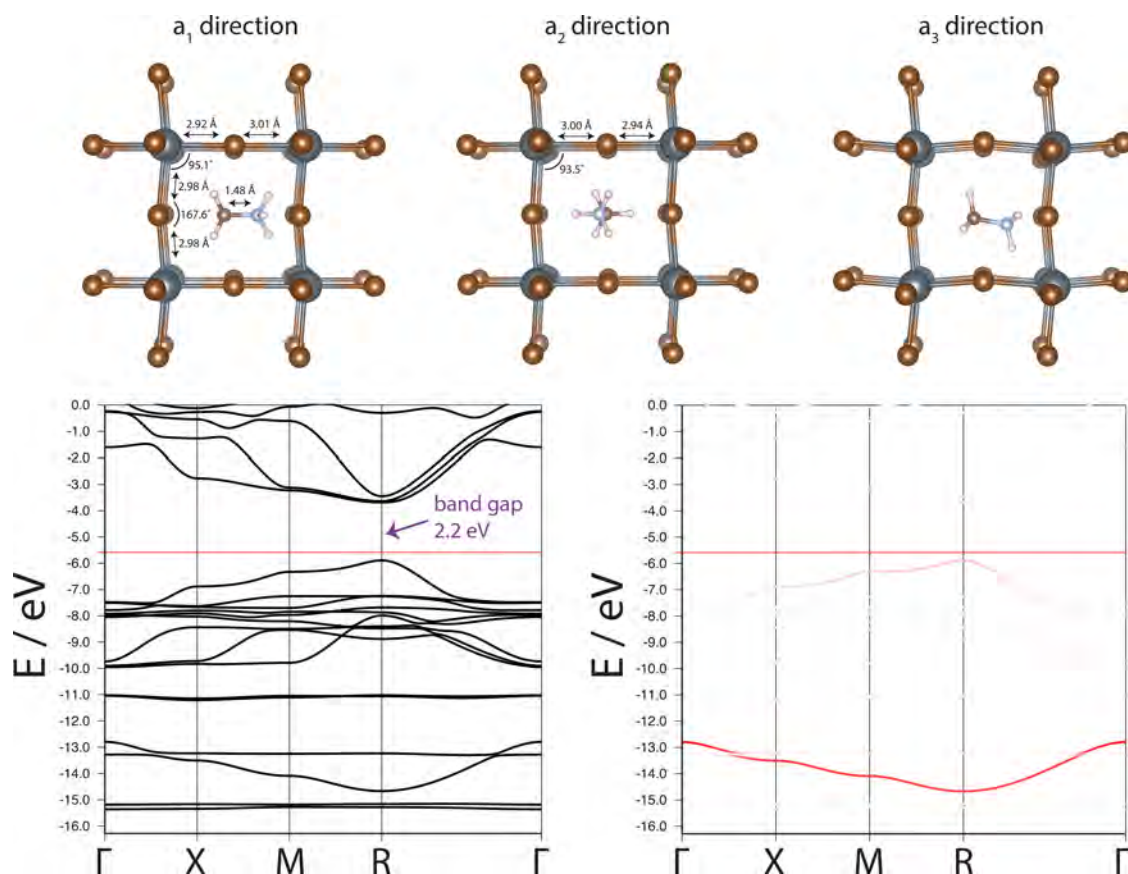**The Mirror Is Robust and Predictive.** We briefly move to the popular hybrid analogue CH$_3$NH$_3$PbBr$_3$, where A ion Cs$^+$

Figure 13. Structure (top) and band structure (bottom, left) of $CH_3NH_3PbBr_3$ with the Pb $6s$ contribution (bottom, right).
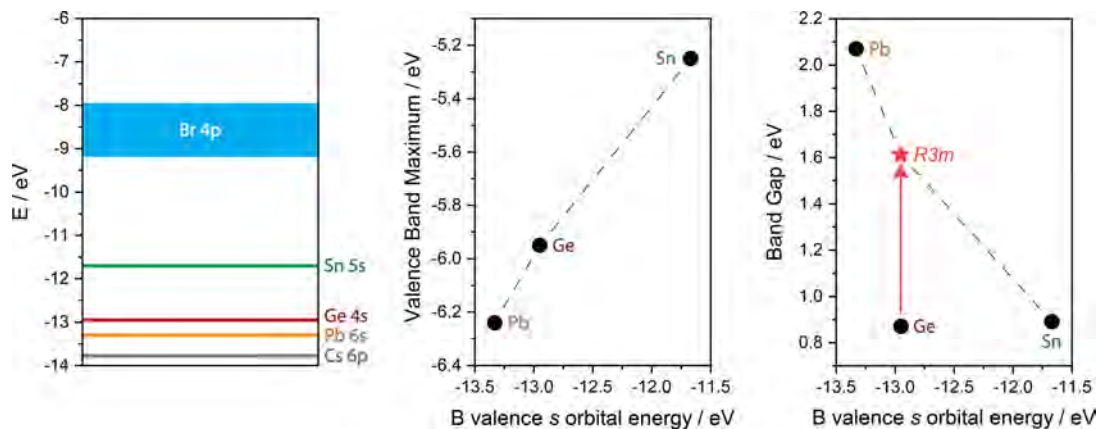

Figure 14. Schematic representation of the Br $4p$ and metal valence s energy levels with the "calibration" Cs $6p$ band (left). Correlation between B metal valence s energy, VBM (middle), and band gap (right).

is replaced by methylammonium. This perovskite is experimentally known to be "pseudocubic" at room temperature: a cube-shaped unit cell that bears a distorted lattice with tilted octahedra.[28,29] The top of Figure 13 displays the structure from three perspectives. Cage-filling $CH_3NH_3^+$ brings some Pb—Br bond length alternation and a departure from the 90° Br—Pb—Br angles. The bottom part of Figure 13 depicts the computed band structure (left), and the Pb $6s$ contribution (right). Note how the flat bands for Cs^+ have made place for several new flat bands with a constant spacing between. These levels belong to the methylammonium ion, which like Cs^+ does not engage in strong chemical bonding; weaker hydrogen-bonding interactions between H(N) atoms and the halide have

been discussed at some length in the literature.[30,31,32] More importantly, the mirror persists, and one may notice how a barely visible decrease in bandwidth for the σ^* increases the band gap by 0.1 eV with respect to $CsPbBr_3$—an effect of the octahedron's distortion giving rise to a slightly diminished Pb—Br σ-interaction.

Varying the B Cation. The mirror does more. Its composition suggests that—given a fixed set of halide ligands, in our case Br—it is the valence metal B ion s orbital that will set the energy value for the valence band maximum (VBM) at R. The closer the energy of this orbital relative to that of Br $4p$, the wider the mirror and the more the σ^* component of the mirror is pushed up. As a consequence, the VBM will lie higher
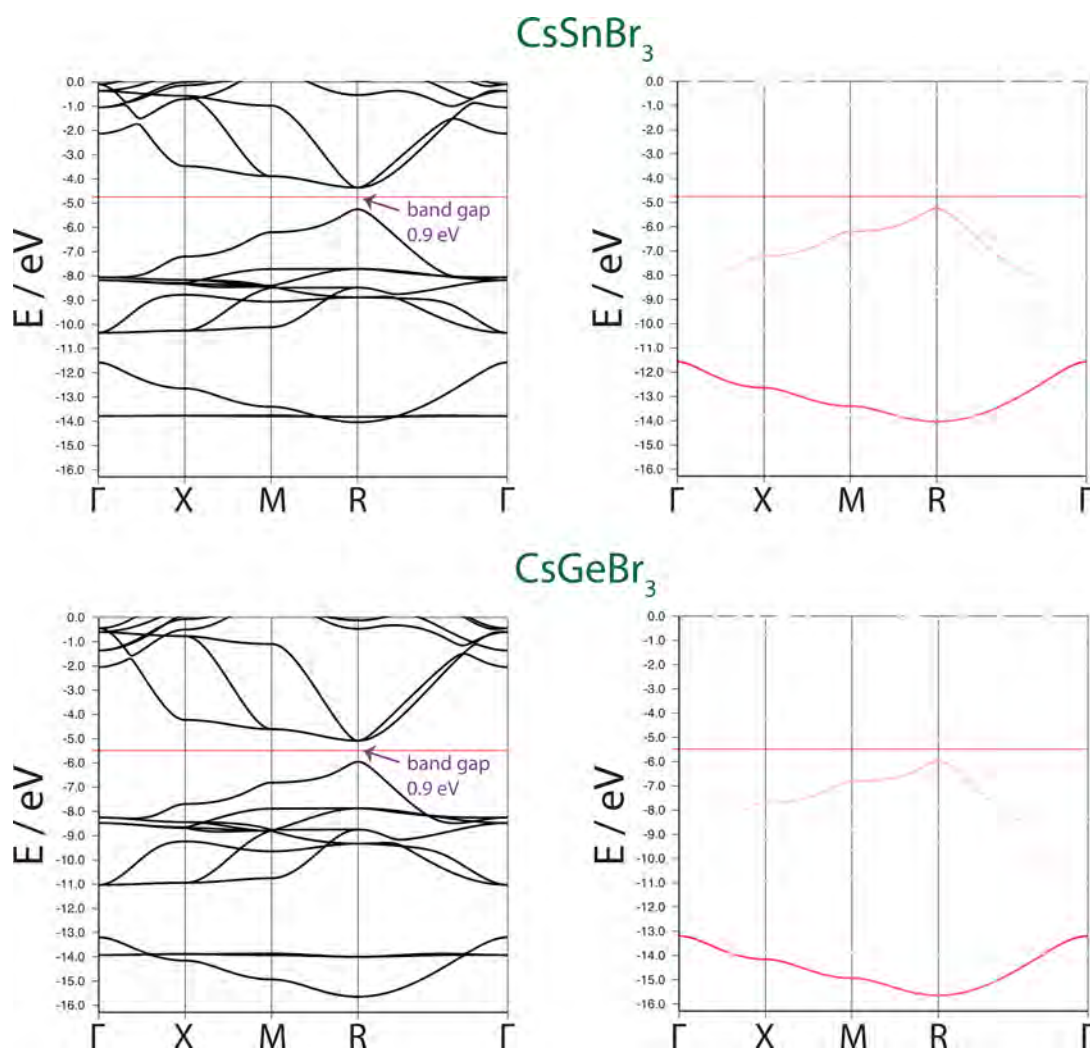
Figure 15. Computed band structures of $Pm\bar{3}m$ CsSnBr$_3$ and CsGeBr$_3$ perovskites; to the right the Pb *6s* contribution.

and narrow the band gap. To demonstrate the validity of this picture, we have optimized CsSnBr$_3$ and CsGeBr$_3$ within cubic symmetry (bond lengths: Sn−Br, 2.95 Å, and Ge−Br, 2.80 Å). The former is a well-investigated perovskite for photovoltaic application as one seeks out lead-free materials. It is experimentally known to be ideally cubic $Pm\bar{3}m$ at room temperature,[33−35] even though a "hidden" distortion at higher temperatures has been recently reported.[36] CsGeBr$_3$ undergoes a distortion toward rhombohedral *R3m*, although the cubic phase can be stabilized by pressure.[37] In Figure 14, the scheme on the left depicts the energies of the B metal valence *s* and Br *4p* levels, as obtained from sublattice calculations (Figure S2). To the right of it, we show the correlation between the metal *s* orbital energy and the VBM, confirming our reasoning: the VBM-B valence energy correlation is almost perfectly linear. The computed band structures for $Pm\bar{3}m$ CsSnBr$_3$ and CsGeBr$_3$—shown in Figure 15 with the Pb *6s* contribution graphed on the right—show the mirror at work, extending the concept we had initially derived by exploring the relativistic effects in CsPbBr$_3$.

The correlation between band gap and metal *s* orbital is not as linear. The gaps of CsPbBr$_3$ and CsSnBr$_3$ are—relatively speaking—where we would expect them; the higher energy of the VBM (with respect to CsPbBr$_3$) narrows the band gap for CsSnBr$_3$, but the one for (virtual) $Pm\bar{3}m$ CsGeBr$_3$ is smaller

than we might predict (Figure 14, right). An inspection of the bands reveals that the conduction band has come to spoil the simple picture, moving down almost 1 eV more than it does for the other two perovskites. But the inescapable distortion toward *R3m* widens the band gap significantly, to 1.62 eV. This typical semiconductor's trait of producing an energy-lowering distortion when the band gap is "too small"[38] pushes, in our case, the value of the gap for CsGeBr$_3$ right between those of CsSnBr$_3$ and CsPbBr$_3$. Even if we would take the distortion toward *Pnma* into account for CsPbBr$_3$ (which slightly widens the computed gap to 2.3 eV, Figure S4), the trend would be there. We intend to explore the mirror's potential in understanding and predicting perovskite distortions separately in the future. For now, we take a look at the way it holds up in *R3m* CsGeBr$_3$.

In *R3m* CsGeBr$_3$, the GeBr$_6$ octahedron sees three Ge−Br bonds stretched to 3.2 Å, and three shortened to about 2.6 Å. We illustrate this in a local view of the octahedral octahedron (Figure 16, top). This deformation from ideally cubic has been described as a Jahn−Teller instability by Seo et al.[39] The BZ for *R3m* is different from the cubic one we have employed before, but it is possible to define a path in the *R3m* BZ that is analogous to the one we had in $Pm\bar{3}m$. It goes from Γ (0,0,0) to Z ($^1/_2$,$^1/_2$,$^1/_2$) through L ($^1/_2$,0,0) and F ($^1/_2$,$^1/_2$,0). The computed band structure along this path (Figure 16, bottom)
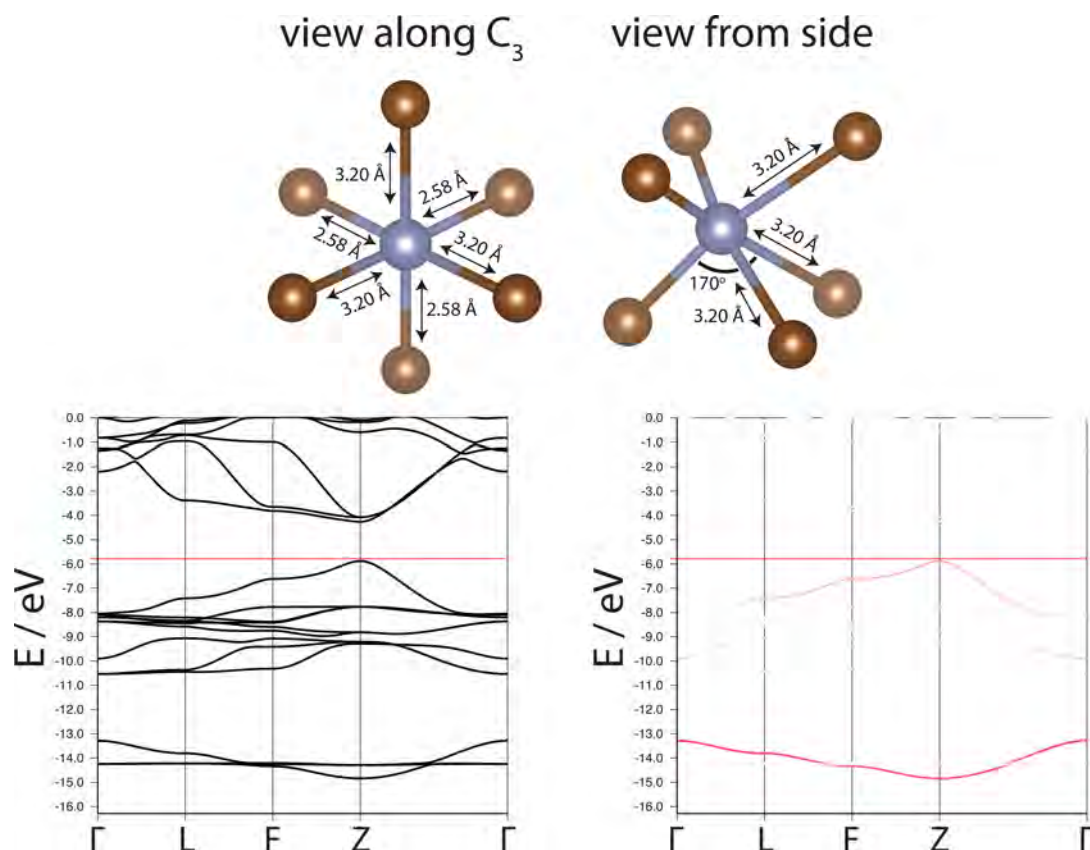
Figure 16. Geometry of the distorted $GeBr_6$ octahedron in $R3m$ $GeGeBr_3$ and the computed band structure with Pb $6s$ contribution.
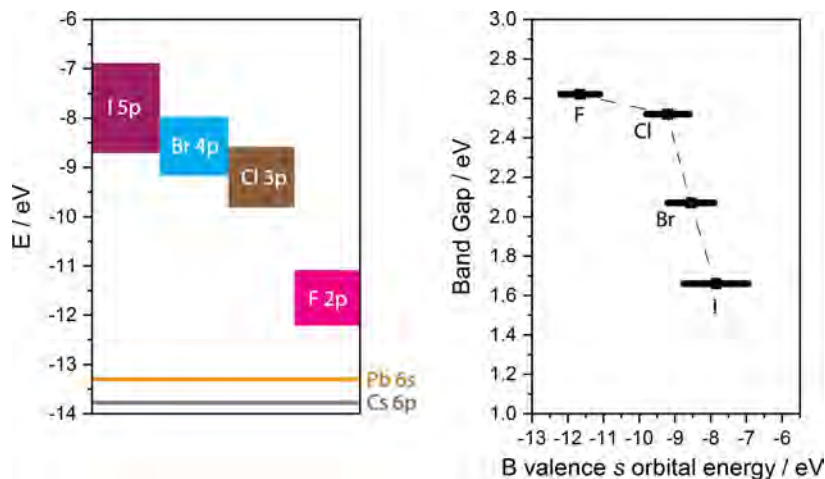

Figure 17. Schematic representation of the halide p and Pb $6s$ energy levels (left), and the correlation between halide p energy and band gap (right).

shows that the mirror is virtually unaffected by the $Pm\overline{3}m$ to $R3m$ distortion, setting the VBM at a value similar to that of cubic $CsPbBr_3$, just above −6 eV. It is the conduction band minimum (CBM) that has moved up in energy to widen the gap; we will provide an understanding of the nature of these bands in an upcoming section.

A Trend for Halides. We have seen how the variation in A and B cations affects (or does not affect) the basic bonding pattern in the structure. A second trend can be anticipated for the halides, tied to their valence p orbital energies. The latter run down in energy on moving up group 17, as graphically depicted in Figure 17 (left). We have optimized $CsPbF_3$,

$CsPbCl_3$, and $CsPbI_3$ within cubic symmetry (bond lengths: Pb−F, 2.33 Å; Pb−Cl, 2.86 Å; Pb−I, 3.19 Å). At experimental room-temperature conditions, $CsPbF_3$ exists as cubic $Pm\overline{3}m$, but distorts to hexagonal $R3c$ at low temperatures (186 K and down).[40,41] $CsPbCl_3$ and $CsPbI_3$ experience the familiar $Pm\overline{3}m$-to-$Pnma$ transition at room temperature,[42,43] which we had earlier mentioned to be there for $CsPbBr_3$ as well. A simple explanation of the extent of this distortion, relating band gap to geometry, is currently not at hand: the distortion is heftier for $CsPbI_3$ than for the bromide and chloride analogues, even though recent experimental progress includes the synthesis of cubic $CsPbI_3$ at lower temperatures than

previously attainable.[44] In describing the trend for the halides, we will stay in ideal cubic symmetry.

Whereas we could predict the trend for the VBM along the series Pb, Sn, and Ge purely on the basis of atomic orbital energies, the picture for the halides is more complex, for two antagonistic factors can be expected to be at work. The σ^* band, that sets the VBM, is predominantly made up by the halide p level. We might then anticipate the VBM to lie higher in energy when we have a higher-lying halide p—this line of thinking would predict the VBM of $CsPbI_3$ to lie highest, and its gap to be smallest. But on the other hand, we can anticipate a decreased strength of interaction with low-lying Pb $6s$ when we push up the energy of the halide p orbitals (as we had in exploring the relativistic effects on $CsPbBr_3$). This would lead to a decrease in splitting for the $PbBr_3$ σ/σ^* pair, and a lower-lying VBM. Molecular calculations on O_h PbX_6 (X = F, Cl, Br, I), exploring the fragment molecular orbital overlap between the a_{1g} linear combination of X p orbitals and Pb $6s$, indicate that these overlaps at our optimized geometries are virtually independent of the halide (0.30–0.31 for all cases, Table S1). We may thus expect the bandwidth to be controlled entirely by the difference in energy levels between the halide p and Pb $6s$. And if the bandwidth is the dominant factor in setting the band gap, we would expect the latter to be smallest for $CsPbF_3$.

The right-hand side of Figure 17 depicts the relationship between the band gap and the halide p energies, which were obtained from sublattice calculations (Figure S3). It shows that the absolute energy value of the halide p orbitals, rather than the interaction with Pb $6s$, is dominant. The trend is linear along I−Br−Cl, but the gap for $CsPbF_3$ is smaller than an extrapolation of this linear relationship would lead one to expect. The computed band structures (Figure S5) are in convincing agreement with what we had argued before, and summarized in Figure 12: the Pb $6s$ mixes increasingly into the σ^* component of the mirror interaction as the halide p drops toward the Pb $6s$ level. The latter is only marginally involved in the σ^* component of the flat mirror for $CsPbI_3$, becomes more of a factor in the same band for $CsPbCl_3$, and is almost equally involved in the σ and σ^* components for $CsPbF_3$, a sign of highly covalent bonding. The details of the Pb−halogen interaction (Figure S5) also show how the close energy resonance of F $2p$ and Pb $6s$ leads to a steep increase in width for the mirror as compared to the case of $CsPbCl_3$, pushing up the σ^* band and VBM significantly.

The Conduction Band: A Second Mirror. For all band structures we have seen until now, the lowest-lying state above the Fermi level is at R. And for all band structures, we can find three conduction bands that create a signature pattern along Γ-X-M-R: two lozenges that resemble the Pb $6p$ pattern of Figure 5 in energy and shape, but which dip down at R. This dip is important, as it creates a direct band gap. The lozenges form a mirror of their own, with a slightly distorted reflection in the halide p band region below the Fermi level. Figure 18 gives a schematic representation of what can be seen explicitly in Figures 4, 13, 15, and 16 (or for that matter in many band structures in the literature).

In trying to understand the crystal orbitals responsible for this second mirror, we start from two observations: (i) the reflected lozenges are made up by three bands at each side of the reflection, that start out from the same energy at Γ and return to the same energy at R; (ii) the components of the mirror lie in regimes of p^{Pb}−p^{halide} interaction, bonding below the Fermi level and antibonding above it (Figure 11, p-p
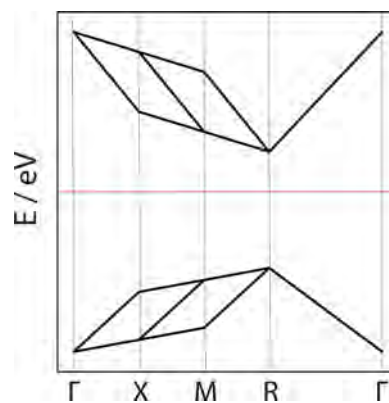

Figure 18. A schematic of the second mirror-like pattern.

COOP). It is clear that the crystal orbitals making up these lozenges consist of the three B metal valence p orbitals in bonding and antibonding combinations with three combinations of halide p orbitals. The only bases that would lead to a triple degeneracy occurring *only* at Γ and R are shown in Figure 19. Note how there is a bonding combination in which
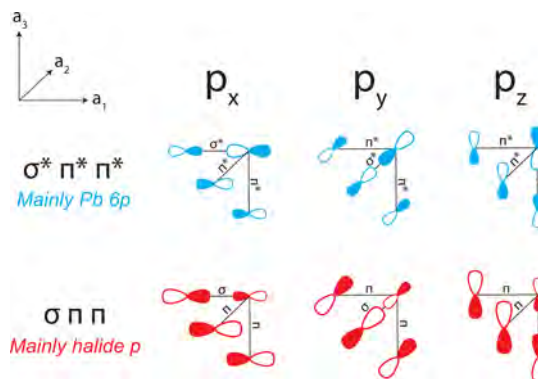

Figure 19. Six orbital bases: three $\sigma\,\pi\,\pi$ and $\sigma^*\,\pi^*\,\pi^*$ Pb $6p$/halide p combinations.

the three combinations are identical, just oriented differently along the three crystallographic directions (this also applies for the three antibonding combinations).

Designating the B metal as "B" and the halide as "X", note also that each basis contains two distinct kinds of B−X bonding: σ and π. The type of interaction is indicated along the bonds. This aspect will be crucial to our understanding—σ-type interactions tend to be substantially larger than π-type interactions, a result of greater overlap. In analogy to our first mirror, where we just had a σ and σ^* basis, we will refer to three bases as $\sigma\,\pi\,\pi$ and to the other three as $\sigma^*\,\pi^*\,\pi^*$.[45] The halide p lies in all cases considerably lower in energy than the Pb $6p$, so the former contributes more to occupied $\sigma\,\pi\,\pi$ and the latter more to the higher-lying and vacant $\sigma^*\,\pi^*\,\pi^*$.

From the bases, we construct the crystal orbitals for the different high-symmetry points of the Brillouin zone. Let us consider just one orbital type for now, p_x, and analyze in detail how the bonding changes along Γ-X-M-R for the $\sigma\,\pi\,\pi$ and $\sigma^*\,\pi^*\,\pi^*$ bands which it makes up. In Figure 20, we follow the representation we had used before—that of a PbX_6 octahedron, where we color the bases red for $\sigma\,\pi\,\pi$ and blue for $\sigma^*\,\pi^*\,\pi^*$. At Γ, translation of the $\sigma\,\pi\,\pi$ basis (without phase factor) along a_1 creates an additional Pb−halide σ
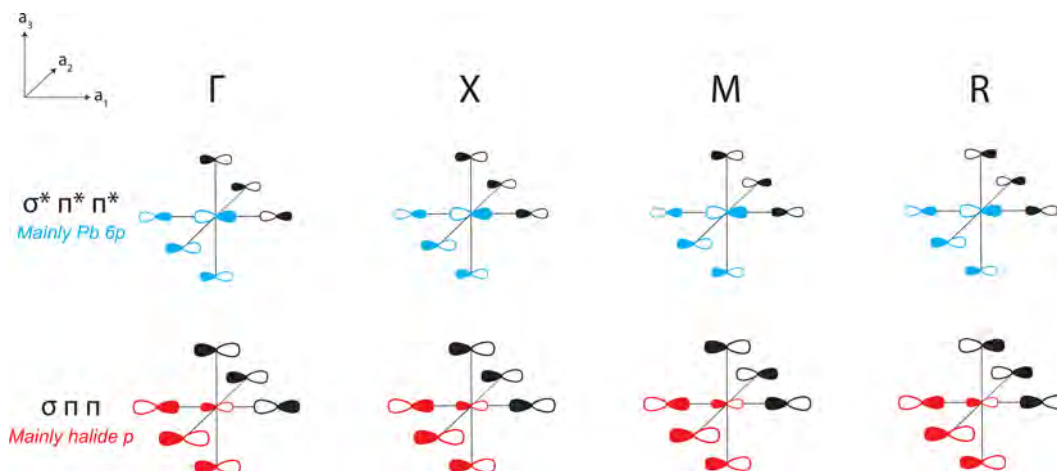
Figure 20. p_x combinations of the $\sigma\ \pi\ \pi$ and $\sigma^*\ \pi^*\ \pi^*$ crystal orbitals along Γ-X-M-R, represented by the PbX_6 octahedral unit. The bases are colored red and blue.

interaction along that axis. Analogously, translations along the a_2 and a_3 axes give rise to two additional π interactions. Note how the $\sigma\ \pi\ \pi$ octahedron at Γ in Figure 21 thus comprises two
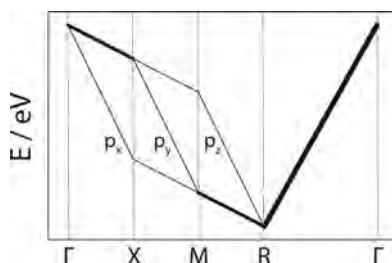

Figure 21. Atomic orbital nature of the $\sigma^*\ \pi^*\ \pi^*$ bands that set the lowest point of the conduction band. Bands degenerate in energy are represented by thicker lines.

σ- and four π-type interactions, a maximally bonding setting. For the $\sigma^*\ \pi^*\ \pi^*$ band, the three translations continue the bonding relationships of that basis—the octahedron in Figure 20 contains two σ^*- and four π^*-type interactions. The $\sigma^*\ \pi^*\ \pi^*$ band is an all-antibonding reflection of $\sigma\ \pi\ \pi$ at Γ, and the splitting between the bands is at its maximum at that point. The second mirror begins its reflection.

Let us describe what happens to the higher-lying (conduction band) $\sigma^*\ \pi^*\ \pi^*$ combination of the p_x orbitals as we move along Γ-X-M-R. The phase inversion at X changes a σ^* interaction to a σ—a significant stabilization—and the band in question moves quite a bit down. On moving to M, a π stabilization replaces a π^* one; the band moves down again, but (much) less so than along Γ-X. This second, smaller stabilization occurs a second time along M-R, and at R it reaches the CBM. The $\sigma^*\ \pi^*\ \pi^*$ band of the p_x orbital runs as indicated in Figure 21.

If one repeats this process for the p_y and p_z $\sigma^*\ \pi^*\ \pi^*$ combinations—the crystal orbitals of which are shown in Figure 22—one obtains similar behavior. The larger changes (occasioned by σ^* interactions changing to σ) occur in predictable sections of the BZ. These are the segments in our path that bring phase inversion along the σ-bonding component in the bases: along a_2 for p_y and along a_3 for p_z.

The pattern of the three $\sigma^*\ \pi^*\ \pi^*$ bands in Figure 21 is mirrored by the runs of the three $\sigma\ \pi\ \pi$ bands (σ/σ^* and π/π^*

exchange in the above argument). But most significantly, we understand the CBM at R: while relatively weak, it is the π-component in the $\sigma^*\ \pi^*\ \pi^*$ bands that sets it and, crucially, establishes a direct band gap. To put it in another way, if there were no π interaction, the energies of the lowest unfilled crystal orbitals—the bottom of the conduction band—would be identical at X, M, and R.

Note how the bonding of the three $\sigma\ \pi\ \pi$ and three $\sigma^*\ \pi^*\ \pi^*$ bands came forth in the p-p contribution of the COOP in Figure 11 (for $CsPbBr_3$). At its lowest point in energy, the (green) p-p curve below the Fermi has its bonding maximum, and becomes nonbonding toward the highest point in energy. Above the Fermi level, the p-p curve goes from nonbonding to progressively antibonding as we move up in energy.

In our treatment of the first mirror, we had analyzed how the VBM depends on the valence orbital energies of the interacting metal B s and halide p. In the same way, we look how the energy of the metal B p orbital correlates with the CBM of the ideally cubic structures in $CsPbBr_3$, $CsSnBr_3$, and $CsGeBr_3$. Figure 23, in which the metal B p orbital energies are obtained from sublattice calculations, shows that this correlation is there. This fits what we would predict, as the CBM is nonbonding and of dominant metal B valence p character. Yet, we consider a tuning of the CBM to be challenging: the variation along the valence p energies for main-group metals is relatively small, and significant spin−orbit effects can be expected for the lower conduction bands when the heavier B metals are involved (Figure S6).[46−48]

A reviewer has pointed out that Figure 23 seems to imply that Ge^{2+} is easier to reduce to Ge^0 than Pb^{2+} to Pb^0. This is not correct. Inclusion of spin−orbit coupling (which we will discuss in further work) brings this trend into better agreement with experiment.

Things Undone. What we have not said a word about are the atomic size considerations (ionic radii) that have dominated much of the literature discussion, allowing people to make reasonable judgements of the potential existence of perovskite structures—we are referring to the Tolerance Factor of Goldschmidt,[49] its applications,[50,51] and recent extensions[52] and alternatives.[53]

In a way, size considerations are contained in the quantum mechanical calculations that we have done: the core of F^- is smaller than that of I^-, ditto for Sn^{2+} relative to Pb^{2+}, and the
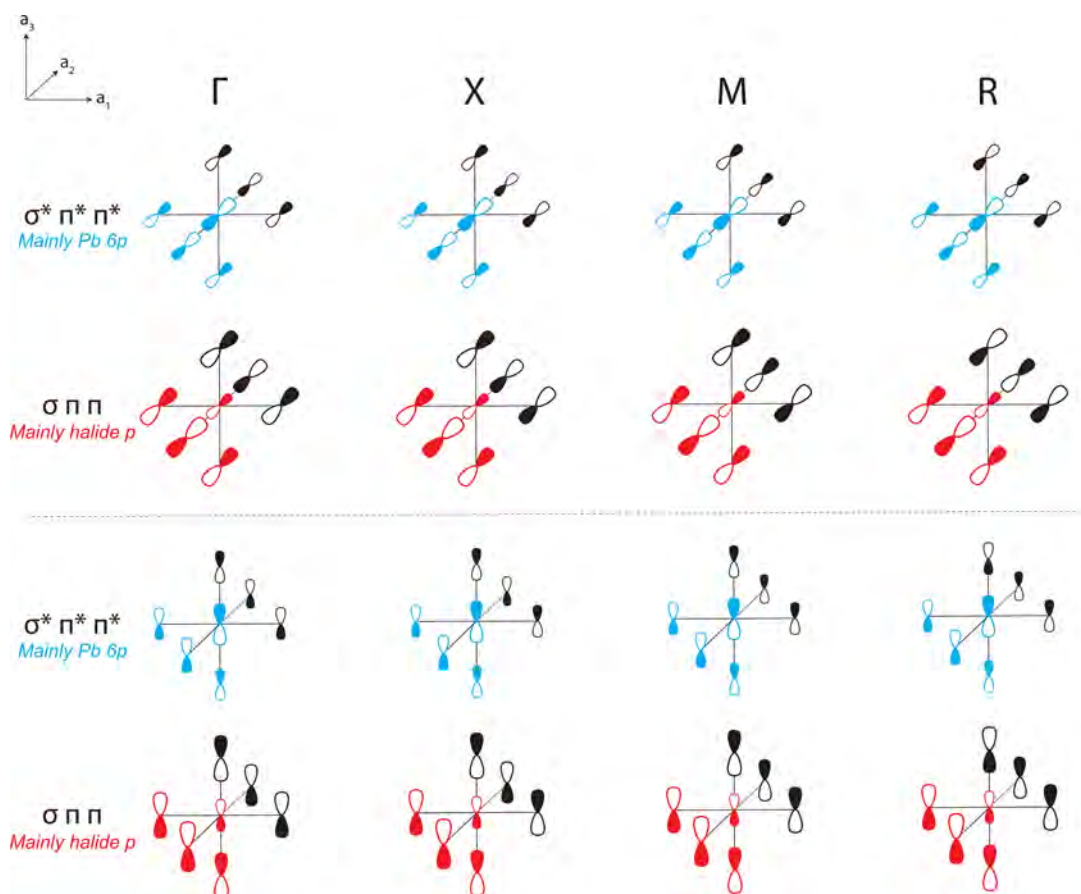
Figure 22. p_y (top) and p_z (bottom) combinations of the $\sigma\,\pi\,\pi$ and $\sigma^*\,\pi^*\,\pi^*$ crystal orbitals along Γ-X-M-R.
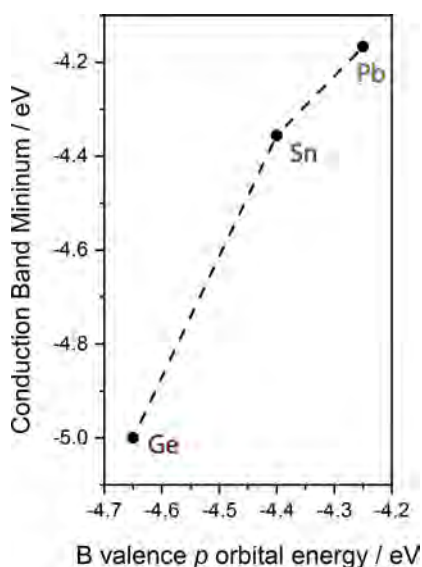

Figure 23. Correlation between B metal valence p energy and the CBM.

equilibrium length of a chemical bond is determined by a balance between attractive and repulsive forces. B and X ions with larger cores will give rise to BX_3 networks with larger lattice constants—in other words, these ions set the size of the cubic cage in which the A cation resides. The A cation can be too large to fill the cage, preventing the octahedral network from existing, or it can be too small, inducing a (sometimes

dynamic) distortion to maximize its electrostatic interaction with the negatively charged BX_3 scaffold.

We have skimped on most of the discussion of geometrical perturbations, in particular on Jahn−Teller distortions and other symmetry-lowering deformations. Certainly, more can be said about local octahedral coordination and lattice distortions, in particular when it comes to connecting these to the chemical bonding model that we have here established. If we have not discussed the ion-size-derived approaches, it is not because they lack utility. To the contrary, they have provided much structural insight. We concentrate on orbitals, symmetry, and bonding because they ultimately underlie geometry.

■ CONCLUSION

This paper provides a bonding analysis for metal halide perovskites in which we relate the magnitude and nature of the band gap to chemical bonding. This is done over an energy range spanning more than 15 eV around the Fermi level.

The changes in the electronic band structure induced by varying the elements that make up ABX_3 are considerable. Yet, they can be well understood in the qualitative way where understanding resides. Two mirrors emerge in the band structure as robust signposts of chemical bonding and antibonding. Atomic orbitals and their interactions control the energy ranges of these mirrors in setting the band gap; how they do so is within the grasp of a chemist's understanding.

If understanding is really there, it should bring predictive and analytical power. Always in the qualitative sense, for hard numbers require high-level calculations, and grasping the essence of computational results typically becomes more

elusive as the calculations become more involved and accurate. The road has been a long one, but we believe it has provided empowering understanding. We would like to take an unusual step by leaving the reader with two problems that will test his or her understanding:

1. If we introduce a group 12 dication, such as Cd^{2+} or Hg^{2+}, what is likely to happen to the band gap, and what role will scalar relativistic effects play?

2. If one goes from $CsPbBr_3$ to $CaTiO_3$, the archetypal and "first" perovskite, how may we expect the general aspects of the bonding and band structure in cubic symmetry to differ from what we have labored to understand for the halides?

We believe we have put into readers' minds the way to answer these (and other) qualitative questions on the bonding in different classes of perovskites.

COMPUTATIONAL METHODS

The crystal structure of $CH_3NH_3PbBr_3$ was taken from ref 28. For all other structures, Quantum Espresso 6.0 was employed for the geometry optimization, using density functional theory.[54,55] We used the Hartwigsen−Goedecker−Hutter scalar-relativistic pseudo-potentials, with a plane-wave cutoff energy of 200 Ry. Band structure, DOS, and COOP calculations on the optimized structures were performed with the ADF BAND package, at the ZORA-SCAN/TZ2P level of theory.[56] In these periodic calculations, we have expanded all wave functions through a Slater-type orbital (STO) basis set. This brings the following advantages with respect to the typical plane-wave calculation.

(i) Atomic orbital contributions to the wave function are obtained directly from the basis set, rather than from projections. The STO functions are as close as we can get to "real" atomic orbitals.

(ii) All-electron basis sets are used, avoiding the use of pseudo-potentials and effective core potentials. Relativistic effects are taken into account by the scalar zeroth-order relativistic approximation (ZORA). By using the same basis set with and without ZORA, we can directly isolate the relativistic contribution to the band structure, and understand these in terms of (Slater-type) atomic orbitals. This will be important in the analysis of heavy-atom perovskites, such as those containing Pb.

The SCAN functional gives reasonable accuracy at limited computational cost.[57] More accurate band gaps can be computed by using hybrid functionals with a screened Coulomb potential, such as HSE06.[58] The qualitative understanding that we have provided in this work does not depend on the functional—Table S2 of the SI demonstrates this.

ASSOCIATED CONTENT

ⓢ Supporting Information

The Supporting Information is available free of charge on the ACS Publications website at DOI: 10.1021/jacs.8b08038.

Figures S1−S6 and Tables S1 and S2, including a comparison of relativistic and non-relativistic COOP for $Pm\bar{3}m$ $CsPbBr_3$, sublattice band structures ($Pm\bar{3}m$ $CsGeBr_3$, $CsSnBr_3$, $CsPbF_3$, $CsPbCl_3$, and $CsPbI_3$), band structure of $Pnma$ $CsPbBr_3$ and of $Pm\bar{3}m$ $CsPbF_3$, $CsPbCl_3$, and $CsPbI_3$, full relativistic band structure of $Pm\bar{3}m$ $CsPbBr_3$, fragment MO overlaps between X_6^{6-} and B^{2+} from a molecular computation on the O_h BX_6^{4-} ion, band gap comparison at PBE, SCAN, and HSE06 levels, and crystal coordinates of the primary structures computed (PDF)

AUTHOR INFORMATION

Corresponding Authors
*mg963@cornell.edu
*rh34@cornell.edu

ORCID 🄾

Maarten G. Goesten: 0000-0003-1296-0255
Roald Hoffmann: 0000-0001-5369-6046

Notes

The authors declare no competing financial interest.

REFERENCES

(1) Lotsch, B. V. New Light on an Old Story: Perovskites Go Solar. *Angew. Chem., Int. Ed.* **2014**, *53* (3), 635.

(2) Stranks, S. D.; Snaith, H. J. Metal-halide perovskites for photovoltaic and light-emitting devices. *Nat. Nanotechnol.* **2015**, *10* (5), 391.

(3) Green, M. A.; Ho-Baillie, A. Perovskite Solar Cells: The Birth of a New Era in Photovoltaics. *ACS Energy Lett.* **2017**, *2* (4), 822.

(4) Kovalenko, M. V.; Protesescu, L.; Bodnarchuk, M. I. Properties and potential optoelectronic applications of lead halide perovskite nanocrystals. *Science* **2017**, *358* (6364), 745.

(5) Manser, J. S.; Saidaminov, M. I.; Christians, J. A.; Bakr, O. M.; Kamat, P. V. Making and Breaking of Lead Halide Perovskites. *Acc. Chem. Res.* **2016**, *49* (2), 330.

(6) Filip, M. R.; Eperon, G. E.; Snaith, H. J.; Giustino, F. Steric engineering of metal-halide perovskites with tunable optical band gaps. *Nat. Commun.* **2014**, *5*, 5757.

(7) Yang, R. X.; Skelton, J. M.; da Silva, E. L.; Frost, J. M.; Walsh, A. Spontaneous Octahedral Tilting in the Cubic Inorganic Cesium Halide Perovskites CsSnX 3and CsPbX 3(X = F, Cl, Br, I). *J. Phys. Chem. Lett.* **2017**, *8* (19), 4720.

(8) Peng, W.; Miao, X.; Adinolfi, V.; Alarousu, E.; El Tall, O.; Emwas, A.-H.; Zhao, C.; Walters, G.; Liu, J.; Ouellette, O.; Pan, J.; Murali, B.; Sargent, E. H.; Mohammed, O. F.; Bakr, O. M. Engineering of $CH_3NH_3PbI_3$ Perovskite Crystals by Alloying Large Organic Cations for Enhanced Thermal Stability and Transport Properties. *Angew. Chem., Int. Ed.* **2016**, *55* (36), 10686.

(9) Gao, W.; Gao, X.; Abtew, T. A.; Sun, Y.-Y.; Zhang, S.; Zhang, P. Quasiparticle band gap of organic-inorganic hybrid perovskites: Crystal structure, spin-orbit coupling, and self-energy effects. *Phys. Rev. B: Condens. Matter Mater. Phys.* **2016**, *93* (8), 085202.

(10) Cardenas-Daw, C.; Simon, T.; Stolarczyk, J. K.; Feldmann, J. Migration of Constituent Protons in Hybrid Organic−Inorganic Perovskite Triggers Intrinsic Doping. *J. Am. Chem. Soc.* **2017**, *139* (46), 16462.

(11) Hirotsu, S.; Harada, J.; Iizumi, M.; Gesi, K. Structural Phase Transitions in $CsPbBr_3$. *J. Phys. Soc. Jpn.* **1974**, *37* (5), 1393.

(12) Stoumpos, C. C.; Malliakas, C. D.; Peters, J. A.; Liu, Z.; Sebastian, M.; Im, J.; Chasapis, T. C.; Wibowo, A. C.; Chung, D. Y.; Freeman, A. J.; Wessels, B. W.; Kanatzidis, M. G. Crystal Growth of the Perovskite Semiconductor CsPbBr 3: A New Material for High-Energy Radiation Detection. *Cryst. Growth Des.* **2013**, *13* (7), 2722.

(13) Poglitsch, A.; Weber, D. Dynamic disorder in methylammo-niumtrihalogenoplumbates (II) observed by millimeter-wave spec-troscopy. *J. Chem. Phys.* **1987**, *87* (11), 6373.

(14) Noh, J. H.; Im, S. H.; Heo, J. H.; Mandal, T. N.; Seok, S. I. Chemical Management for Colorful, Efficient, and Stable Inorganic−Organic Hybrid Nanostructured Solar Cells. *Nano Lett.* **2013**, *13* (4), 1764.

(15) Burdett, J. K. *Chemical bonding in solids*; Oxford University Press, 1995.

(16) Miao, M.-S. Caesium in high oxidation states and as a p-block element. *Nat. Chem.* **2013**, *5* (10), 846.

(17) Rogachev, A. Y.; Miao, M.-S.; Merino, G.; Hoffmann, R. Molecular CsF$_5$ and CsF$_2$. *Angew. Chem., Int. Ed.* **2015**, *54* (28), 8275.

(18) Goesten, M. G.; Rahm, M.; Bickelhaupt, F. M.; Hensen, E. J. M. Cesium's Off-the-Map Valence Orbital. *Angew. Chem., Int. Ed.* **2017**, *56* (33), 9772.

(19) Huang, L.-Y.; Lambrecht, W. R. L. Electronic band structure, phonons, and exciton binding energies of halide perovskites CsSnCl$_3$, CsSnBr$_3$, and CsSnI$_3$. *Phys. Rev. B: Condens. Matter Mater. Phys.* **2013**, *88* (16), 165203.

(20) Giorgi, G.; Fujisawa, J.-I.; Segawa, H.; Yamashita, K. Cation Role in Structural and Electronic Properties of 3D Organic–Inorganic Halide Perovskites: A DFT Analysis. *J. Phys. Chem. C* **2014**, *118* (23), 12176.

(21) Endres, J.; Egger, D. A.; Kulbak, M.; Kerner, R. A.; Zhao, L.; Silver, S. H.; Hodes, G.; Rand, B. P.; Cahen, D.; Kronik, L.; Kahn, A. Valence and Conduction Band Densities of States of Metal Halide Perovskites: A Combined Experimental–Theoretical Study. *J. Phys. Chem. Lett.* **2016**, *7* (14), 2722.

(22) Hoffmann, R. Interaction of orbitals through space and through bonds. *Acc. Chem. Res.* **1971**, *4* (1), 1.

(23) The real and reciprocal space vectors are related by $a_i \cdot b_i = 2\pi$, $b_i = 2\pi/a_i$. As the special points are located halfway the reciprocal-lattice vector (a Wigner–Seitz cell), the coordinates in terms of the real-space lattice constant a are Γ (0,0,0), X (π/a,0,0), M ($\pi/a,\pi/a$,0), and R ($\pi/a,\pi/a,\pi/a$).

(24) Hoffmann, R. How Chemistry and Physics Meet in the Solid State. *Angew. Chem., Int. Ed. Engl.* **1987**, *26* (9), 846.

(25) When we consider the interaction of two orbitals of different initial energies e_1^0 and e_2^0, the energies of the two new orbitals can be derived as $e_1 = e_1^0 + (H_{12} - e_1^0 S_{12})^2/(e_1^0 - e_2^0)$ and $e_2 = e_2^0 + (H_{12} - e_2^0 S_{12})^2/(e_2^0 - e_1^0)$. The second term in the equation, the one that carries the effects of interaction, has in its numerator a term that can be related to orbital overlap, and in the denominator a term that—if setting e_1^0 lower in energy than e_2^0—is negative for e_1 and positive for e_2. The consequence is stabilization and destabilization of the initial levels, respectively. An increase in energy difference between e_1^0 and e_2^0 leads to a vanishing of the second term, reducing in the limit e_1 to e_1^0 and e_2 to e_2^0. Albright, T. A.; Burdett, J. K.; Whangbo, M.-H. *Orbital Interactions in Chemistry*, 2nd ed.; Wiley, 2013.

(26) Wolfram, T.; Ellialtıoğlu, Ş. *Electronic and Optical Properties of d-Band Perovskites*; Cambridge University Press, 2006.

(27) Wolfram, T.; Ellialtıoğlu, Ş. *Applications of Group Theory to Atoms, Molecules, and Solids*; Cambridge University Press, 2014.

(28) Butler, K. T.; Frost, J. M.; Walsh, A. Band alignment of the hybrid halide perovskites CH$_3$NH$_3$PbCl$_3$, CH$_3$NH$_3$PbBr$_3$ and CH$_3$NH$_3$PbI$_3$. *Mater. Horiz.* **2015**, *2* (2), 228.

(29) Yin, T.; Fang, Y.; Fan, X.; Zhang, B.; Kuo, J.-L.; White, T. J.; Chow, G. M.; Yan, J.; Shen, Z. X. Hydrogen-Bonding Evolution during the Polymorphic Transformations in CH$_3$NH$_3$PbBr$_3$: Experiment and Theory. *Chem. Mater.* **2017**, *29* (14), 5974.

(30) Amat, A.; Mosconi, E.; Ronca, E.; Quarti, C.; Umari, P.; Nazeeruddin, Md. K.; Grätzel, M.; De Angelis, F. *Nano Lett.* **2014**, *14*, 3608.

(31) Svane, K. L.; Forse, A. C.; Grey, C. P.; Kieslich, G.; Cheetham, A. K.; Walsh, A.; Butler, K. T. How Strong Is the Hydrogen Bond in Hybrid Perovskites? *J. Phys. Chem. Lett.* **2017**, *8* (24), 6154.

(32) El-Mellouhi, F.; Marzouk, A.; Bentria, E. T.; Rashkeev, S. N.; Kais, S.; Alharbi, F. H. Hydrogen Bonding and Stability of Hybrid Organic-Inorganic Perovskites. *ChemSusChem* **2016**, *9* (18), 2648.

(33) Barrett, J.; Bird, S. R. A.; Donaldson, J. D.; Silver, J. The Mössbauer effect in tin(II) compounds. Part XI. The spectra of cubic trihalogenostannates(II). *J. Chem. Soc. A* **1971**, *0* (0), 3105.

(34) Parry, D. E.; Tricker, M. J.; Donaldson, J. D. The electronic structure of CsSnBr$_3$ and related trihalides; Studies using XPS and band theory. *J. Solid State Chem.* **1979**, *28* (3), 401.

(35) Gupta, S.; Bendikov, T.; Hodes, G.; Cahen, D. A Lead-Free Halide Perovskite for Long-Term Solar Cell Application: Insights on SnF$_2$ Addition. *ACS Energy Lett.* **2016**, *1* (5), 1028.

(36) Fabini, D. H.; Laurita, G.; Bechtel, J. S.; Stoumpos, C. C.; Evans, H. A.; Kontos, A. G.; Raptis, Y. S.; Falaras, P.; Van der Ven, A.; Kanatzidis, M. G.; Seshadri, R. Dynamic Stereochemical Activity of the Sn^{2+} Lone Pair in Perovskite CsSnBr$_3$. *J. Am. Chem. Soc.* **2016**, *138* (36), 11820.

(37) Schwarz, U.; Hillebrecht, H.; Kaupp, M.; Syassen, K.; von Schnering, H. G.; Thiele, G. Pressure-Induced Phase Transition in CsGeBr$_3$ Studied by X-Ray Diffraction and Raman Spectroscopy. *J. Solid State Chem.* **1995**, *118* (1), 20.

(38) Burdett, J. K.; Coddens, B. A.; Kulkarni, G. V. Band gap and stability of solids. *Inorg. Chem.* **1988**, *27* (18), 3259.

(39) Seo, D. K.; Gupta, N.; Whangbo, M. H.; Hillebrecht, H.; Thiele, G. Pressure-Induced Changes in the Structure and Band Gap of CsGeX$_3$ (X = Cl, Br) Studied by Electronic Band Structure Calculations. *Inorg. Chem.* **1998**, *37* (3), 407.

(40) Berastegui, P.; Hull, S.; Eriksson, S.-G. A low-temperature structural phase transition in CsPbF$_3$. *J. Phys.: Condens. Matter* **2001**, *13* (22), 5077.

(41) Smith, E. H.; Benedek, N. A.; Fennie, C. J. Interplay of Octahedral Rotations and Lone Pair Ferroelectricity in CsPbF$_3$. *Inorg. Chem.* **2015**, *54* (17), 8536.

(42) Linaburg, M. R.; McClure, E. T.; Majher, J. D.; Woodward, P. M. Cs$_{1-x}$Rb$_x$PbCl$_3$ and Cs$_{1-x}$Rb$_x$PbBr$_3$ Solid Solutions: Understanding Octahedral Tilting in Lead Halide Perovskites. *Chem. Mater.* **2017**, *29* (8), 3507.

(43) Trots, D. M.; Myagkota, S. V. High-temperature structural evolution of caesium and rubidium triiodoplumbates. *J. Phys. Chem. Solids* **2008**, *69* (10), 2520.

(44) Swarnkar, A.; Marshall, A. R.; Sanehira, E. M.; Chernomordik, B. D.; Moore, D. T.; Christians, J. A.; Chakrabarti, T.; Luther, J. M. Quantum dot-induced phase stabilization of α-CsPbI$_3$ perovskite for high-efficiency photovoltaics. *Science* **2016**, *354* (6308), 92.

(45) The σ and σ^* bands of our first mirror could also be referred to as $\sigma\,\sigma\,\sigma$ and $\sigma^*\,\sigma^*\,\sigma^*$, respectively.

(46) Azarhoosh, P.; McKechnie, S.; Frost, J. M.; Walsh, A.; van Schilfgaarde, M. Research Update: Relativistic origin of slow electron-hole recombination in hybrid halide perovskite solar cells. *APL Mater.* **2016**, *4* (9), 091501.

(47) Zheng, F.; Tan, L. Z.; Liu, S.; Rappe, A. M. Rashba Spin–Orbit Coupling Enhanced Carrier Lifetime in CH$_3$NH$_3$PbI$_3$. *Nano Lett.* **2015**, *15* (12), 7794.

(48) Brenner, T. M.; Egger, D. A.; Kronik, L.; Hodes, G.; Cahen, D. Hybrid organic—inorganic perovskites: low-cost semiconductors with intriguing charge-transport properties. *Nat. Rev. Mater.* **2016**, 15007.

(49) Goldschmidt, V. M. Die Gesetze der Krystallochemie. *Naturwissenschaften* **1926**, *14* (21), 477.

(50) Li, Z.; Yang, M.; Park, J.-S.; Wei, S.-H.; Berry, J. J.; Zhu, K. Stabilizing Perovskite Structures by Tuning Tolerance Factor: Formation of Formamidinium and Cesium Lead Iodide Solid-State Alloys. *Chem. Mater.* **2016**, *28* (1), 284.

(51) Tsui, K. Y.; Onishi, N.; Berger, R. F. Tolerance Factors Revisited: Geometrically Designing the Ideal Environment for Perovskite Dopants. *J. Phys. Chem. C* **2016**, *120* (40), 23293.

(52) Sun, Q.; Yin, W.-J. Thermodynamic Stability Trend of Cubic Perovskites. *J. Am. Chem. Soc.* **2017**, *139* (42), 14905.

(53) Travis, W.; Glover, E. N. K.; Bronstein, H.; Scanlon, D. O.; Palgrave, R. G. On the application of the tolerance factor to inorganic and hybrid halide perovskites: a revised system. *Chem. Sci.* **2016**, *7* (7), 4548.

(54) Giannozzi, P.; Baroni, S.; Bonini, N.; Calandra, M.; Car, R.; Cavazzoni, C.; Ceresoli, D.; Chiarotti, G. L.; Cococcioni, M.; Dabo, I.; Dal Corso, A.; de Gironcoli, S.; Fabris, S.; Fratesi, G.; Gebauer, R.; Gerstmann, U.; Gougoussis, C.; Kokalj, A.; Lazzeri, M.; Martin-Samos, L.; Marzari, N.; Mauri, F.; Mazzarello, R.; Paolini, S.; Pasquarello, A.; Paulatto, L.; Sbraccia, C.; Scandolo, S.; Sclauzero, G.; Seitsonen, A. P.; Smogunov, A.; Umari, P.; Wentzcovitch, R. M.

QUANTUM ESPRESSO: a modular and open-source software project for quantum simulations of materials. *J. Phys.: Condens. Matter* **2009**, *21* (39), 395502.

(55) Giannozzi, P.; Andreussi, O.; Brumme, T.; Bunau, O.; Buongiorno Nardelli, M.; Calandra, M.; Car, R.; Cavazzoni, C.; Ceresoli, D.; Cococcioni, M.; Colonna, N.; Carnimeo, I.; Dal Corso, A.; de Gironcoli, S.; Delugas, P.; DiStasio, R. A., Jr; Ferretti, A.; Floris, A.; Fratesi, G.; Fugallo, G.; Gebauer, R.; Gerstmann, U.; Giustino, F.; Gorni, T.; Jia, J.; Kawamura, M.; Ko, H.-Y.; Kokalj, A.; Küçükbenli, E.; Lazzeri, M.; Marsili, M.; Marzari, N.; Mauri, F.; Nguyen, N. L.; Nguyen, H.-V.; Otero-de-la-Roza, A.; Paulatto, L.; Poncé, S.; Rocca, D.; Sabatini, R.; Santra, B.; Schlipf, M.; Seitsonen, A. P.; Smogunov, A.; Timrov, I.; Thonhauser, T.; Umari, P.; Vast, N.; Wu, X.; Baroni, S. Advanced capabilities for materials modelling with Quantum ESPRESSO. *J. Phys.: Condens. Matter* **2017**, *29* (46), 465901.

(56) SCM Software for Chemistry & Materials, www.scm.com.

(57) Sun, J.; Ruzsinszky, A.; Perdew, J. P. Strongly Constrained and Appropriately Normed Semilocal Density Functional. *Phys. Rev. Lett.* **2015**, *115*, 036402.

(58) Krukau, A. V.; Vydrov, O. A.; Izmaylov, A. F.; Scuseria, G. E. Influence of the exchange screening parameter on the performance of screened hybrid functionals. *J. Chem. Phys.* **2006**, *125* (22), 224106.